SCIENCE ROBOTICS | RESEARCH ARTICLE

NANOROBOTS

# Mechano-fluorescence actuation in single synaptic vesicles with a DNA framework nanomachine

**Jiangbo Liu[1], Xinxin Jing[2], Mengmeng Liu[3], Fan Li[1], Min Li[1], Qian Li[2], Jiye Shi[4], Jiang Li[4,5], Lihua Wang[4,5], Xiuhai Mao[1]*, Xiaolei Zuo[1,2]*, Chunhai Fan[2]**

**Biomimetic machines that can convert mechanical actuation to adaptive coloration in a manner analogous to cephalopods have found widespread applications at various length scales. At the nanoscale, a transmutable nanomachine with adaptive colors that can sense and mediate cellular or intracellular interactions is highly desirable. Here, we report the design of a DNA framework nanomachine (DFN) that can autonomously change shape in response to pH variations in single synaptic vesicles, which, in turn, displays adaptive fluorescent colors with a mechano-fluorescence actuation mechanism. To construct a DFN, we used a tetrahedral DNA nanostructure as the framework to incorporate an embedded pH-responsive, i-motif sequence tagged with a Förster resonance energy transfer pair and an affinity cholesterol moiety targeting vesicular membranes. We found that endocytosed DFNs are individually trapped in single endocytic vesicles in living synaptic cells due to the size-exclusion effect. The adaptive fluorescence coloration of DFNs enabled single-vesicle quantification of resting pH values in a processive manner, allowing long-term tracking of the exocytosis and fusion dynamics in intracellular processes and cell-cell communications.**

## INTRODUCTION

Biomimetic machines autonomously change their physical properties, such as shape, stiffness, and size, to exert mechanical force or motion in response to certain external stimuli. Integration of diverse functionality and intelligence has led to the development of engineered biological systems with mechanical shape change, adaptive support, and tactile sensing in a fully programmable way (*1*–*4*). In particular, their ability to dynamically change their shape and color to adapt to varied environments inspired the development of transmutable and color-variable machines with artificial intelligence for widespread applications (*5*, *6*). For example, an adaptive infrared-reflecting system that combines the mechanical actuation–induced adaptive coloration and sensing system was developed for infrared camouflage by drawing inspiration from the skin of cephalopods (squid, octopuses, etc.). It is also envisioned that the development of nanoscale biomimetic machines that can actively sense, signal, and transform in response to cellular and organellar environments may revolutionize theranostics and nanomedicine. However, unlike natural protein–based molecular machines (*7*–*9*), the navigating, targeting, and transforming abilities of designer nanomachines that may otherwise function properly in solution are largely hindered by the complexity of cellular and subcellular systems (*10*–*19*), which lays a grand challenge in synthetic nanomachines (*20*, *21*).

During the past decades, a variety of material systems have been developed to realize morphological adaption (*22*–*30*). Among them, the intrinsic precision and programmability of DNA molecules provide a promising approach to designing dynamic DNA frameworks with well-defined and reconfigurable conformational change (*31*–*34*). Intuitively, a biomolecular nanomachine is more compatible with the cellular environment than inorganic nanoparticle– or organic molecule–based ones, as also manifested by the experimental demonstration of designer DNA nanomachines for treating cancers, acute kidney injury, and other diseases (*35*–*38*). Nevertheless, these DNA nanomachines are generally single purposed, whereas the transportation of DNA nanomachines within and across various cellular and subcellular membranes remains practically difficult (*38*, *39*).

In this work, we design a size-adaptive, membrane-targeting DNA framework nanomachine (DFN) in which components with diverse functionality can work in tandem. As a natural example of mechanic actuation, the shape and coloration of cephalopod skin can be changed autonomously and repeatedly for the purpose of signaling, concealing, or transforming to adapt to varied environments, as illustrated for the squid in an octopus pot in fig. S1. In a sense, the skin of cephalopods behaves as a dynamic mechano-coloration machine in which the internal sacculi packed with pigment granules in pigment cells are expanded and contracted through the mechanical actuation of radial muscle cells that, in turn, display varied colors. Analogous to the mechanical actuation–induced adaptive coloration system of cephalopod skin, the DNA framework behaves as a dynamic mechano-coloration machine that expands and contracts to display varied colors in response to certain external stimuli. Moreover, analogous to an octopus pot (fig. S1), we reason that the secretion of endocytosed DFNs, an important step during vesicle fusion, is critically dependent on the size of DFNs (Fig. 1). Given the precise programmability of DFNs, their size and color

---

[1]Institute of Molecular Medicine, Shanghai Key Laboratory for Nucleic Acid Chemistry and Nanomedicine, Renji Hospital, School of Medicine, Shanghai Jiao Tong University, Shanghai 200127, China. [2]School of Chemistry and Chemical Engineering, Zhang Jiang Institute for Advanced Study, Frontiers Science Center for Transformative Molecules and National Center for Translational Medicine, Shanghai Jiao Tong University, Shanghai 200240, China. [3]Shanghai Key Laboratory of Green Chemistry and Chemical Processes, School of Chemistry and Molecular Engineering, East China Normal University, Shanghai 200127, China. [4]Division of Physical Biology, CAS Key Laboratory of Interfacial Physics and Technology, Shanghai Institute of Applied Physics, Chinese Academy of Sciences, Shanghai 201800, China. [5]Interdisciplinary Research Center, Shanghai Synchrotron Radiation Facility, Zhangjiang Laboratory, Shanghai Advanced Research Institute, Chinese Academy of Sciences, Shanghai 201210, China.
*Corresponding author. Email: maoxiuhai@sjtu.edu.cn (X.M.); zuoxiaolei@sjtu.edu.cn (X.Z.)

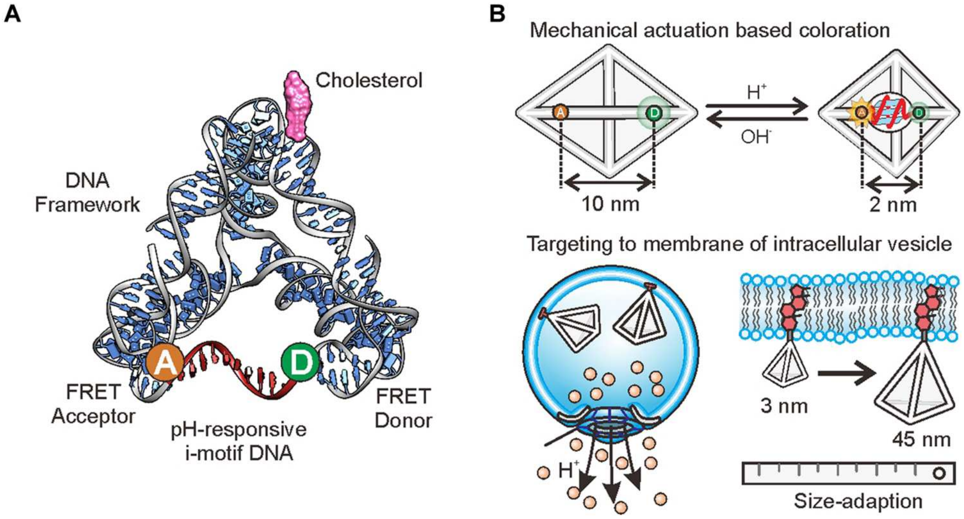

**Fig. 1. Schematic for the design of DFNs with an adaptive size and mechano-fluorescence actuation.** (**A**) Schematic illustration of the design of mechano-fluorescence actuation–based DFNs. The rigid TDF was designed as a nanomachine by embedding a pH-responsive i-motif sequence tagged with a FRET pair onto one edge and an affinity cholesterol moiety. The i-motif was 2.9 nm in height and 2.1 nm in width (Protein Data Bank 1ELN) (*56*). (**B**) DFNs with a mechano-fluorescence actuation mechanism to pH variation in a vesicle. The DFNs consist of three modules: cholesterol moiety for targeting vesicular lipid membrane, a size-adaptive (from 3 to 45 nm) TDF for integrating various functions, and a pH-responsive i-motif underlying mechano-fluorescence actuation in the size (from ~10 to ~2 nm) for FRET-based dynamic coloration.

adaptation to the vesicular lumen environment provide a feasible solution to processive tracking of the dynamics of vesicle fusion in synaptic cells.

## RESULTS

### Biomimetic design and construction of DFNs

We conceptualized a size-adaptive nanomachine using DNA frameworks and functional nucleic acids. The DFN was composed of a size-programmable DNA framework with an embedded pH-responsive i-motif sequence tagged with a Förster resonance energy transfer (FRET) pair and an affinity cholesterol moiety targeting vesicular membranes (Fig. 1). When actuated in response to the acidic pH, the embedded i-motif of a DFN sensed $H^+$ and associated to form the i-tetraplex structure via two parallel-stranded $C–H•C^+$ base-paired duplexes (*15*, *40*, *41*), which resulted in mechanical actuation that contracted the reconfigurable edge of DFNs from 14 to 7 nm in size, converting the DNA framework from an irregular to a regular tetrahedron. Subsequently, the shape transformation led to dipole-dipole coupling between the excited state of the donor and the ground state of the acceptor via FRET, resulting in mechano-fluorescence of the DFN.

### Structural characterization of reconfigurable DNA framework

In this integrated nanomachine, the DNA framework realized the localization and control of these functional domains. The resulting structural DNA framework can then be engineered to make these systems analytically tractable for diverse purposes. Here, we set out to construct a series of tetrahedral DNA frameworks (TDFs) with various length edges, including 7, 20, 26, and 120 base pairs (bp). As revealed by the gel shift assay (figs. S2 and S3), these formed DNA frameworks exhibited one clear band, and the yield was calculated to be ~90%, indicating successful assembly. Atomic force microscopy (AFM) images confirmed the formation of the TDF structures with a characterized three-dimensional tetrahedral morphology (fig. S4), which was consistent with our design. In addition, the dynamic light scattering results indicated that these DNA frameworks exhibited hydrodynamic sizes of 6.8 ± 0.4 nm, 13.8 ± 1.5 nm, 17.1 ± 1.6 nm, and 41.6 ± 2.1 nm for 7, 20, 26, and 120 bp, respectively (fig. S5). Hence, the DNA framework featured a programmable structural size and desired shape.

The DFN was fabricated by tightly integrating pH-responsive i-motif actuation, FRET-based dynamic coloration, and vesicular membrane targeting into the rigid DNA framework. We then asked whether the incorporation of multiple functional nucleic acids into DNA frameworks can result in the integration of diverse functions into DFNs. We first characterized whether the pH-responsive i-motif actuation resulted in the shape transformation of DNA framework. The incorporation of i-motif DNA into one edge transformed it into a reconfigurable DNA framework. In this structure, five edges of this structure were double helices, whereas the sixth edge contained DNA with a reconfigurable i-motif. Because of the nature of the DNA framework's reconfigurable edge, the transformation of the DNA framework can be realized through the actuation of i-motif DNA on the reconfigurable edge (Fig. 2A). As a typical example, a representative 20-bp edged DNA framework was characterized by observing their shape transformations with AFM and transmission electron microscopy (TEM). Before the actuation, both AFM imaging and TEM imaging revealed that the DFNs were of an irregular tetrahedral structure (Fig. 2B and fig. S6), featuring an average diameter of ~14 nm in size and an apparent lateral length of ~13 nm at the i-motif–incorporated reconfigurable edge (Fig. 2B). Upon actuation, the DFN structure was transformed to a regular tetrahedral structure, with its reconfigurable edge shrunk by the pH-actuated i-

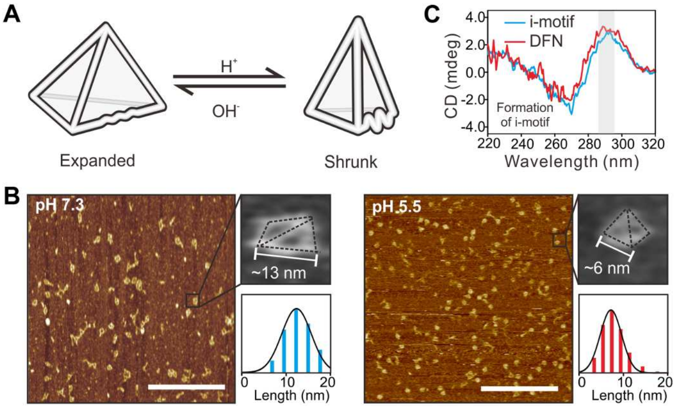

**Fig. 2. Characterization of mechanically actuated DFNs.** (**A**) Schematic illustration of mechanically actuated DFNs with shrunken morphology (pH 5.5) and expanded morphology (pH 7.3). (**B**) AFM imaging and quantification of DFNs with shrunken morphology (pH 5.5) and expanded morphology (pH 7.3), respectively. Scale bars, 200 nm. The apparent lateral length of the i-motif–incorporated reconfigurable edge was 13.1 ± 2.5 nm ($n$ = 34, means ± SD) and 6.4 ± 3.0 nm ($n$ = 34, means ± SD) at pH 7.3 and 5.5, respectively. (**C**) CD spectra of DFN and i-motif. DFN showed a positive peak at 288 nm and a negative peak at 270 nm in the difference spectra between pH 5.5 and 7.3, which is in agreement with the characteristic peaks for i-motif structure.

motif. The corresponding morphologic images showed that the actuated DFNs featured an average diameter of ~7 nm in size and an apparent shrinkage length of ~6 nm at the reconfigurable edge (Fig. 2B and fig. S7). The i-motif actuation could dynamically modulate both the size and the reconfigurable edge by approximately twofold. Moreover, circular dichroism (CD) spectroscopy on the reconfigurable DNA framework revealed that the C-rich DNA sequence in the configurable edge adopted an extended conformation at pH 7.3, whereas, at pH 5.5, it formed the identical i-tetraplex structure of a free C-rich sequence (Fig. 2C and fig. S8). These results indicated that the DFN's shape transformation was due to the pH response of i-motif actuation underlying the reconfigurable edge.

## pH-responsive fluorescent coloration of DFNs

Next, we explored how to control the dynamic coloration of DFNs on the basis of pH-responsive actuation. We labeled the reconfigurable edge with various FRET fluorophore pairs—such as Cy3/Cy5, JOE/TAMRA-N, 6-FAM/TAMRA-N, Alexa 647/BHQ-3, and 6-FAM/BHQ-1—as donor and acceptor, respectively. By modulating the structural transformation of pH-responsive i-motif, we used the variation in the absorbance or fluorescence spectra of the DFNs to sense the environmental change, as shown in Fig. 3A and fig. S9. Using the Cy3/Cy5 dual-tagged DFN as an example, no FRET with fluorescence at the wavelength of Cy5 (650 nm) was observed under Cy3 excitation (570 nm) before actuation in pH 7.3, because Cy3 and Cy5 were separated by the expanded shape (Fig. 3B). After the actuation in an acidic solution (pH 5.5), the DFNs were transmuted to the shrunken state, and an emission at the wavelength of Cy5 was observed with the Cy3 excitation (570 nm) (Fig. 3B). This pH-responsive coloration was further confirmed by total internal reflection fluorescent microscopy (TIRFM) at the single-molecule level (Fig. 3B). Hence, this approach enabled our DFNs with pH-responsive coloration on the basis of the i-motif–actuated structural transformation.

We also probed the pH-sensing performance of the reconfigurable DNA framework by evaluating the pH sensitivity in dynamic coloration as a function of pH value. Variation in the pH value on the Alexa 647/BHQ-3 dual-tagged DFNs changed the ratio of their expanded and shrunken shapes, as shown in Fig. 3C. This resulted in a different Alexa 647 fluorescent signal due to FRET in the shrunken shape after the i-motif actuation. Moreover, a plot of the Alexa 647 fluorescent signal as a function of pH value revealed a standard sigmoid-like calibration curve that featured a sharp increase between pH 6.0 and 7.0 [p$K_a$ (where $K_a$ is the acid dissociation constant) equal to 6.5] and a high apparent Hill coefficient ($n$H; the slope of the fluorescence versus pH curve) of 2.3, which is nearly identical to that of the i-motif–based DNA nanomachine (*42*). This result, in turn, indicated that dynamic coloration originated from the i-motif DNA mechanical actuation in response to pH variation.

We then evaluated the pH-responsive kinetics of DFN by real-time monitoring of the Alexa 647 fluorescent signal in its dynamic coloration. Acid or base was added to the buffer, during which we measured the Alexa 647 fluorescent signal in real time at room temperature. We found that each step of coloration was predominantly completed within 1.0 s (fig. S10). The reaction rate constants for the shape expansion and shrinkage were estimated to be 2.3 and 2.6 $s^{-1}$, respectively (calculated the kinetics of their responsiveness as a first-order reaction), illustrating that the response times of DFN's coloration were fast. Moreover, the changes in the coloration were consistent and fully reversible upon repeated pH cycling between 7.3 and 5.5, with a negligible change in the Alexa 647 fluorescent signal observed after 10 cycles (Fig. 3D). Therefore, the pH-responsive mechanical actuation of DFNs can be effectively translated to FRET variations in response to a specific excitation with negligible influence from the DNA framework.

In addition, we compared the pH-responsive dynamic coloration of DFN with that of previously reported pH sensors for monitoring cellular and organelle environments, such as molecular dye FM 1-43, quantum dot (Qdot), and superecliptic pHluorin (SEP). The treatment of these potential interferences—including $Cu^{2+}$, $Fe^{3+}$, $Ni^{2+}$, $Ca^{2+}$, $Mg^{2+}$, and $Na^{+}$—had a neglectable influence on the Alexa 647 fluorescent signal (Fig. 3E) but substantially reduced the fluorescent signal by 30 to 40% for Qdot (figs. S11 and S12). Meanwhile, the DFN exhibited the highest apparent $n$H among pH probes, allowing for the evaluation of pH change in a very narrow range (Fig. 3F). Moreover, the DFN exhibited the same relative change in fluorescence ($\Delta F/F_{max}$) from pH 5.5 to pH 7.3 as Qdot (with $\Delta F/F_{max}$ of 0.6), which was 67% that of the SEP (with $\Delta F/F_{max}$ of 0.9) and approximately six times that of FM 1-43 (with $\Delta F/F_{max}$ of 0.1) (figs. S13 to S17). This result, in turn, indicated that DFNs were brighter than other probes. Therefore, this mechano-fluorescence–based dynamic coloration enabled DFNs to be well positioned to detect minute pH changes within cellular and organelle environments and might inspire the rational design of probes for monitoring environmental pH variation.

## The targetability of DFNs

In addition to sensing the environmental variation, we investigated whether the structural adaptation of the DNA framework allowed for DFN targeting and transportation within and across diverse

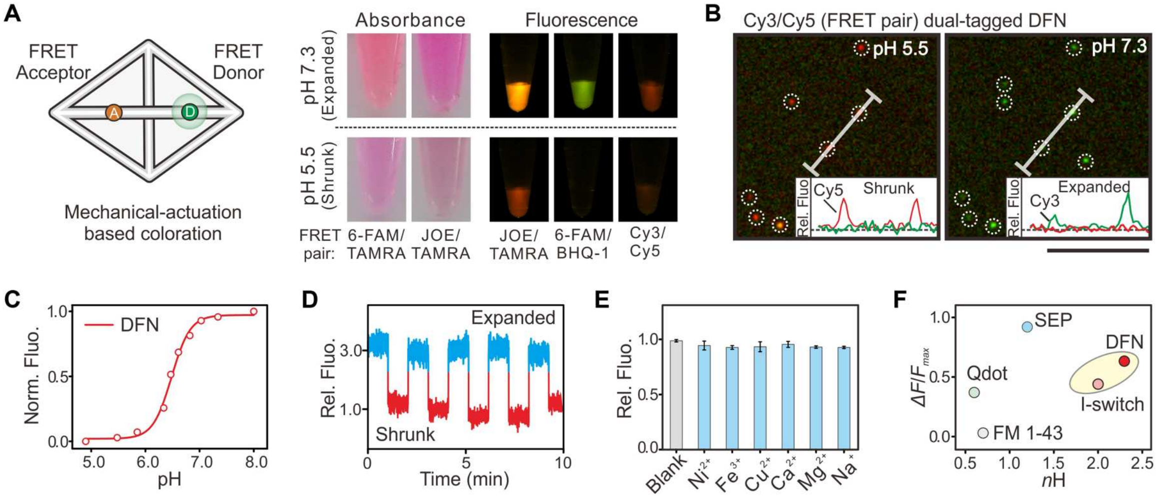

**Fig. 3. Characterization of the dynamic coloration of DFNs.** (**A**) Schematic illustration and imaging of pH-responsive dynamic coloration for DFNs modified with variable FRET pairs. The "Absorbance" columns are bright-field images of the visible colors displayed by visible light absorbance at pH 5.5 and 7.3. The "Fluorescence" columns are images of the fluorescence colors displayed by ultraviolet light exciting at pH 5.5 and 7.3. (**B**) Dynamic coloration of DFNs with Cy3/Cy5 FRET pair in TIRFM images. Scale bar, 10 μm. (**C**) The DFNs' normalized fluorescence intensity (Norm. Fluo.) changes as pH conditions change from acidic to basic. Alexa 647/BHQ-3 were applied as FRET donor and acceptor in the DFN for the experiment. The fluorescence of DFN substantially increased with a sharp slope. (**D**) Characterization of DFNs' fluorescence change during in vitro–repeated operations between pH 5.5 and pH 7.3. Alexa 647/BHQ-3 were applied as FRET donor and acceptor in the DFN for the experiment. (**E**) The DFN relative fluorescence intensity (Rel. Fluo.) in different metal ion solutions ($Ni^{2+}$, $Fe^{3+}$, and $Cu^{2+}$) and biologically relevant ion solutions ($Ca^{2+}$, $Mg^{2+}$, and $Na^{+}$). Alexa 647/BHQ-3 were applied as FRET donor and acceptor in the DFN for the experiment. The error bars represent means ± SD ($n$ = 3). (**F**) The apparent $n$H and relative change in fluorescence ($\Delta F/F_{max}$) of DFN, Qdot, I-switch, SEP, and FM 1-43, respectively. $\Delta F$ is the fluorescence intensity difference between pH 5.5 and pH 7.3; $F_{max}$ is the fluorescence intensity at pH 7.3.

cellular and subcellular membranes. In particular, intracellular vesicle lumenal pH changes are essential for organelle function and integral to cellular processes such as endocytosis and exocytosis. Then, we sought to anchor DFNs within the vesicle and monitor lumenal pH changes of the intracellular vesicle. We modified a cholesterol moiety at the corner via DNA hybridization (Fig. 4A and fig. S18). This strategy enabled DFNs with attachment to living cells under varied environments. We confirmed the attachment of DFNs to living cells by imaging rat pheochromocytoma (PC12) cells after incubating cholesterol-labeled DFNs with cells at various concentrations (fig. S19, A and B). After analyzing these DFN-tagged PC12 cells using flow cytometry (Fig. 4B), we found that the fluorescence intensity of the DFNs adhering to the cells followed a standard sigmoid-like dependence on the DFN concentration, with a maximum fluorescence intensity at a concentration of about 300 nM (fig. S19C). These results confirmed that the DFN attachment was not due to nonspecific adsorption but due to the hydrophobic interaction between cholesterol and the inner lipid of the membrane. Figure 4C depicts a typical confocal laser scanning microscopy (CLSM) image of PC12 cells after 15 min of incubation with 200 nM DFNs. Our Cy3/Cy5 doubly labeled DFNs exhibited green fluorescence upon excitation with Cy3 and were found to be localized to the cell surface membrane. To explore the function of the DFNs at the lipid membrane surface in the living cells, we next incubated these tagged cells in an acidic solution (pH 5.5) for periods of 30 min. The Cy3 and Cy5 labels of the DFNs remained colocalized on the cell surface membrane (Fig. 4C and fig. S20), indicating the integrity of the DFNs. Meanwhile, in agreement with the in vitro coloration experiments, our DFNs exhibited FRET fluorescence (red) of Cy5 upon Cy3 excitation at the cell surface membrane, illustrating the fidelity of the dynamic coloration in varied environments of living cells.

Next, we studied the transportation of DNA nanomachines within and across various cellular and subcellular membranes. The capability of cholesterol-modified DNA frameworks as an uptake ligand was exploited to specifically encapsulate and deliver them to endocytic vesicles (Fig. 4D). The PC12 cells were incubated with a mixture of DFNs and FM 1-43, a widely used fluorescent dye for labeling vesicles in vivo (*43*), and imaged in a CLSM (Fig. 4E and fig. S21). The DFNs were found to be localized in distinct intracellular structures in the CLSM images, whereas DFNs without cholesterol moiety modification barely entered the cells (fig. S22). This further suggested the importance of cholesterol moiety modification in the targeting module of DFNs. When these images were overlaid with cointernalized FM 1-43 images, these spots were found to colocalize (Fig. 4E and fig. S23), indicating that the DFNs had entered the intracellular vesicle. To further characterize the location of intracellular DFNs relative to the vesicle, we used DNA hybridization to modify DFNs with 10-nm gold nanoparticles (AuNPs) (fig. S24). Using TEM images, we observed that the DFN-tagged AuNPs were attached to the vesicle's inner surface (Fig. 4F), indicating that DFNs were endocytotically overriden and attached to the vesicle's inner membrane. Moreover, we found that DFNs had a negligible effect on cell health by using a calcein acetoxymethyl ester (calcein-AM) staining assay and real-time cellular analysis (figs. S25 and S26).

We also investigated whether DFNs were transported into the intracellular exocytotic vesicle (Fig. 5A). The PC12 cells containing DFNs were incubated in 90 mM $K^{+}$ and imaged over the time required for vesicle exocytosis (*43*, *44*). As revealed by the fluorescence images, the colocalization spots of our DFNs and FM 1-43

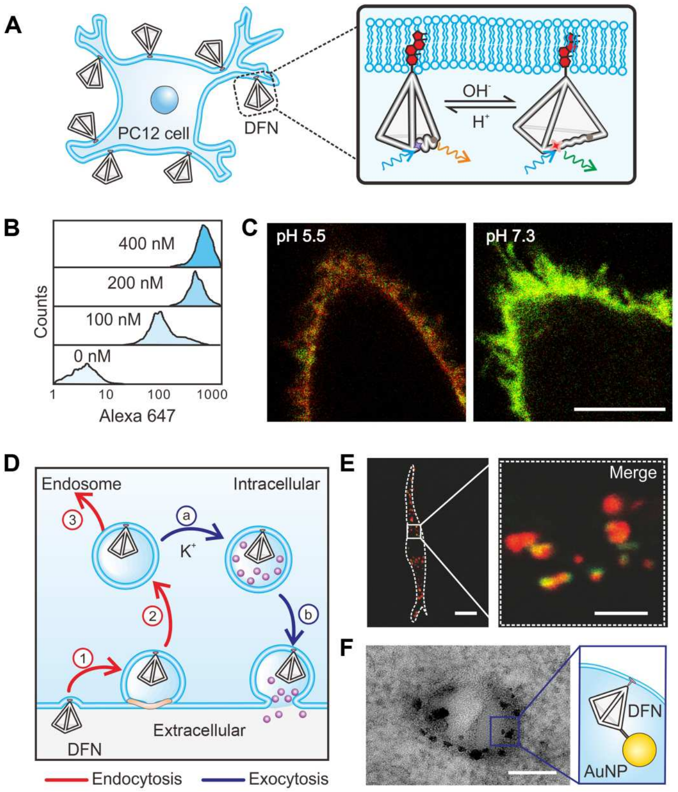

**Fig. 4. Cholesterol-induced attachment of DFNs to intracellular vesicles.** (**A**) Schematic illustration of DFN attachments to the PC12 cell membrane by cholesterol modification. (**B**) Flow cytometry analysis for DFNs attaching to cell membranes. (**C**) CLSM imaging for DFNs attaching to cell membranes. Cy3/Cy5 doubly labeled DFNs were used. Scale bar, 10 μm. (**D**) Scheme for DFN entry into a synaptic vesicle. (**E**) CLSM imaging of vesicles with FM 1-43 staining and DFN loading in PC12 cells. Alexa 647–modified DFNs were used. Scale bars, 20 μm (zoomed out) and 5 μm (zoomed in). (**F**) Scheme and TEM imaging of DFN-AuNP distributed inside the vesicle. Scale bar, 50 nm.

migrated to the outer cell membrane (Fig. 5B and fig. S27), demonstrating that our DFNs were amenable to imposing an endocytosis and exocytosis program via the vesicle cycle.

Next, we explored the effect of size adaption over the fusion pore on the targeting of DFN during dynamic vesicle fusion. For instance, the optimal particle size for targeting the vesicular lumen requires that the particles be small enough to fit within the vesicular lumen but large enough to be rejected by putative fusion pores (*13*, *44*–*48*). We programmed the prepared Alexa 647–modified DFNs with three geometrically increased sizes—~3-nm DFN-1, ~10-nm DFN-2, and ~45-nm DFN-3 (fig. S4)—and analyzed their fluorescence intensity variations during vesicle fusion. As revealed by the CLSM images, no fluorescence variation was observed in DFN-3 (figs. S28 to S30), most likely because its size was too large to fit within the exocytic vesicle's lumen. In contrast, the fluorescence of both DFN-1 and DFN-2 decreased after the vesicle fused with the cellular membrane (figs. S27 and S31). Furthermore, we discovered that the distribution of fluorescence decreases for both DFN-1 and DFN-2 fell into two distinct categories: a leakage category with fluorescence decreases of above 50%, corresponding to DFNs escaping the vesicle, and a stay category with fluorescence decreases of less than 50%, corresponding to DFNs staying inside the vesicle (fig. S32). We further calculated the ratio of leakage categories and found that the DFN-2 had a lower leakage ratio than the DFN-1 (Fig. 5, C and D). This may result from the putative fusion pores rejecting larger DFNs due to the size exclusion effect.

To substantiate the effect of size adaptation on the fate of our DFNs during vesicle fusion, we designed an i-motif (~3 nm), an i-motif–based DNA nanomachine (I-switch with ~8 nm in size), and two sizes of fixed-size and configuration DNA frameworks (shrinking corresponding to ~6-nm-diameter shrunken DFN-2 and expanding corresponding to ~12-nm-diameter expanded DFN-2) and evaluated their fluorescence variation (figs. S33 to S39). It was also found that the leakage ratios decreased in size in a hyperbola-like fashion (Fig. 5, C and D). The size-dependent lumenal fate of DFNs indicated that our DFN-2 can be localized to the desired subcellular compartment without causing reporter loss during the multiple fusion processes. Therefore, by encapsulating themselves in a single vesicle, the DFNs not only imposed an endocytosis and exocytosis program but also suggested a possible application as imaging probes for determining fusion dynamics.

## Tracking vesicle fusion dynamics

Next, we explored the use of DFNs to distinguish the exocytotic vesicle fusion dynamics (Fig. 6A), which underpins the study of cellular functions and communications, including transmembrane signaling, intracellular transport, and cell migration and division. Vesicle exocytosis shows characteristic pH variation profiles that are integral to vesicle release patterns, including the full-collapse fusion (FCF) mode, in which vesicles flatten completely into the plasma membrane and eventually lose their identity, and "kiss-and-run" (K&R), in which vesicles transiently fuse with and retrieve the plasma membrane (*44*–*48*). When exocytic vesicles fuse with the surface membrane of cells, they undergo a characteristic pH increase from 5.5 to 7.3 in the FCF mode and a transient pH cycling between 5.5 and 7.3 in the K&R mode (*44*, *45*). SEP has been used extensively for imaging single-vesicle exocytosis because of its nearly optimal p$K_a$ (7.3) and high $n$H (1.2). Before vesicles fused with the cellular membrane, however, negligible SEP fluorescence was observed (*49*). Moreover, either a low signal-to-noise ratio or a low apparent $n$H for FM 1-43 and Qdot left the vesicle fusion dynamics in synaptic cells uncertain (*44*).

The coloration module of the DFN allowed for the detection of minute pH variations with high sensitivity and specificity. Moreover, its size-adaptative DNA framework module allowed it to meet the required size, which was small enough to fit into the vesicular lumen but large enough to be rejected by putative K&R fusion pores. Then, we used DFN-2 to monitor and track the fluorescence intensity of exocytic vesicles loaded with DFNs in PC12 cells in situ. By using the time-dependent fluorescence profile, we observed a burst ~35% ($\Delta F/F$, fig. S40) in the fluorescence trace, as shown in Fig. 6B. This was a result of the exocytosis vesicle with our DFN and FM 1-43 being transferred from the acidic intracellular environment (pH 5.5) to the weakly neutral extracellular medium (pH 7.3). In particular, the amplitudes of the upticks were distinct from baseline noise (fig. S41), allowing us to distinguish the K&R mode from the FCF mode. After that, the fluorescence intensity for DFNs decreased. Then, we discovered two distinct patterns: a transient positive deflection (uptick) ~15% above baseline, corresponding to the K&R mode, and an uptick immediately followed by a negative step

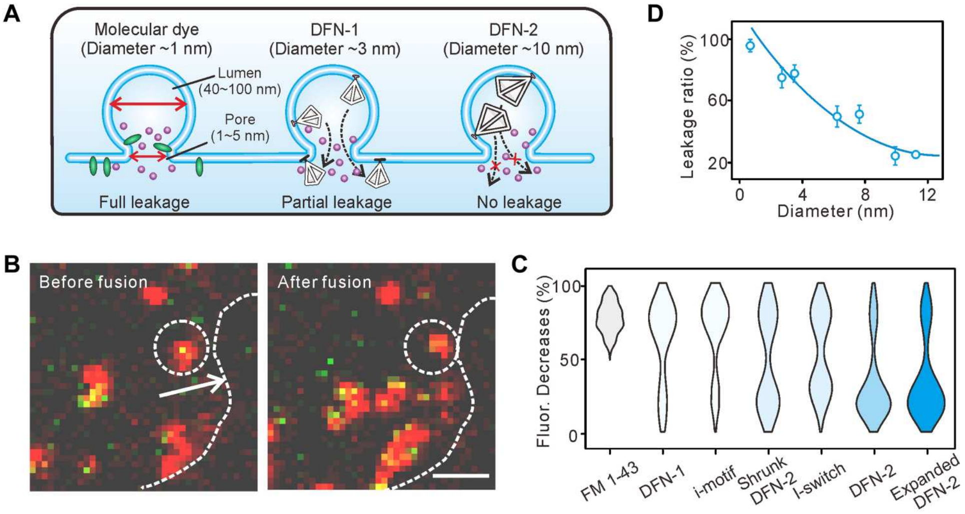

**Fig. 5. Size-dependent cellular fates of DFNs.** (**A**) Schematic illustration for the effect of a DFN's size adaptation on its fate in a PC12 cellular vesicle. Alexa 647–modified DFNs and I-switch were used. (**B**) CLSM images of a DFN-2 that barely moved outside of the vesicle with FM 1-43. Scale bar, 1 μm. (**C**) Violin plot of fluorescence decrease (*n* = 122, 60, 42, 176, 75, 75, and 184 for FM 1-43, DFN-1, i-motif, shrunk DFN-2, I-switch, DFN-2, and expanded DFN-2, respectively). (**D**) Normalization leakage ratio for FM 1-43, I-switch, and size-adaptive DFNs (0.95, 0.74, 0.77, 0.48, 0.49, 0.21, and 0.22 for FM 1-43, DFN-1, i-motif, shrunk DFN-2, I-switch, DFN-2, and expanded DFN-2, respectively). Circumcircle diameters of different DFNs were used. The error bars represent means ± SEM (*n* = 3).

(downstep), corresponding to the FCF mode (*44*). Furthermore, these dynamic patterns of fusion were observed in other neurocyte cells, such as Neuro-2a and SH-SY5Y (figs. S42 and S43), indicating the versatility of DFNs in detecting the dynamic motion of vesicles.

Having established the capability of DFNs to accurately determine the exocytotic vesicle fusion dynamics between FCF and K&R modes, we next analyzed the fluorescence intensity trace of DFNs in each tagged fusion vesicle, allowing us to quantify the fusion dynamics of released vesicles in PC12 cells. After analyzing 148 vesicles fusing with the surface membrane upon $K^+$ stimulation, we observed various combinations of fusion modes: 47 for one fusion time (28 for single K&R and 19 for FCF), 35 for two fusion times (24 for double K&R and 11 for single K&R + FCF), 37 for three fusion times (30 for triple K&R and 7 for double K&R + FCF), and 29 for tetrad K&R (Fig. 6, C and D). Knowing the amount of each fusion mode, we found that the K&R ratio increased with the number of fusion times (Fig. 6E). This was likely because vesicles with a higher probability of release (performed more fusion times) prefer K&R (*44*). In addition, we investigated the relationship between the latency of the initial fusion and the time interval between subsequent fusions for various fusion modes. Statistical analysis of single-vesicle photoluminescence revealed that as the number of fusions increased, the latency time for the first fusion and the interval fusion time decreased (Fig. 6F and figs. S44 and S45). These findings demonstrated that the mechano-fluorescence–based dynamic coloration of DFNs can act as a processive sensor for environmental variation and thus reveal their dynamic functionality.

## DISCUSSION

We have designed adaptive DFNs with mechano-fluorescence properties in response to pH variation and framing size to adapt to various environments. First, our DFNs replicate a critical natural capability of mechano-coloration and adaptive appearance. The DFNs can frame their size to adapt to the microenvironment. Moreover, similar to the mechanical actuation–based dynamic coloration, the autonomous color change enables an ultrasensitive and rapid response to cellular or intracellular interactions.

Furthermore, the nanomachine's intrinsic and accurate response allows for the demonstration of vesicle lipid membrane locomotion. This essentially makes the nanomachine a powerful tool for in situ monitoring of fusion dynamics. Although previous protein-based sensors avidly bind to specific receptors, they have limited size and shape programmability to adapt to the lumenal size of the vesicle, because they can easily escape through the fusion pore (*47*). Whereas pH-sensitive Qdot probes are attractive due to their programmable size and pH-dependent photoluminescence change, they cannot anchor tightly to the membrane (*50*–*52*). In contrast, our DFNs combine the advantages of pH-responsive mechano-fluorescence actuation with size programmability, thereby satisfying the critical requirements of robust membrane association and pH sensitivity. By optimizing the size of the DNA framework, we can create nanomachines with identical sensor characteristics that fit within the vesicular lumen and can be localized to any desired subcellular compartment without sacrificing reporters during the multiple fusion processes. As a proof of concept, we can now study the entire process of exocytosis and how the fusion dynamics regulate their functionality by monitoring the resting pH of individual vesicles.

We also note that nanomachine systems are designed to facilitate a wide range of applications, including in situ monitoring and analysis of fusion dynamics across multiple systems. Currently, our DFNs are capable of determining the pH variation within a vesicle. However, before they can be widely used as in vivo DNA-based molecular machines, certain limitations need to be overcome. A sensing module that can respond to different chemical or physical stimuli—such as dopamine, $Ca^{2+}$, and $Zn^{2+}$—needs to be designed and incorporated (*29*). In addition to probing intracellular pH variation and vesicle fusion dynamics, our DFNs can mimic the diverse

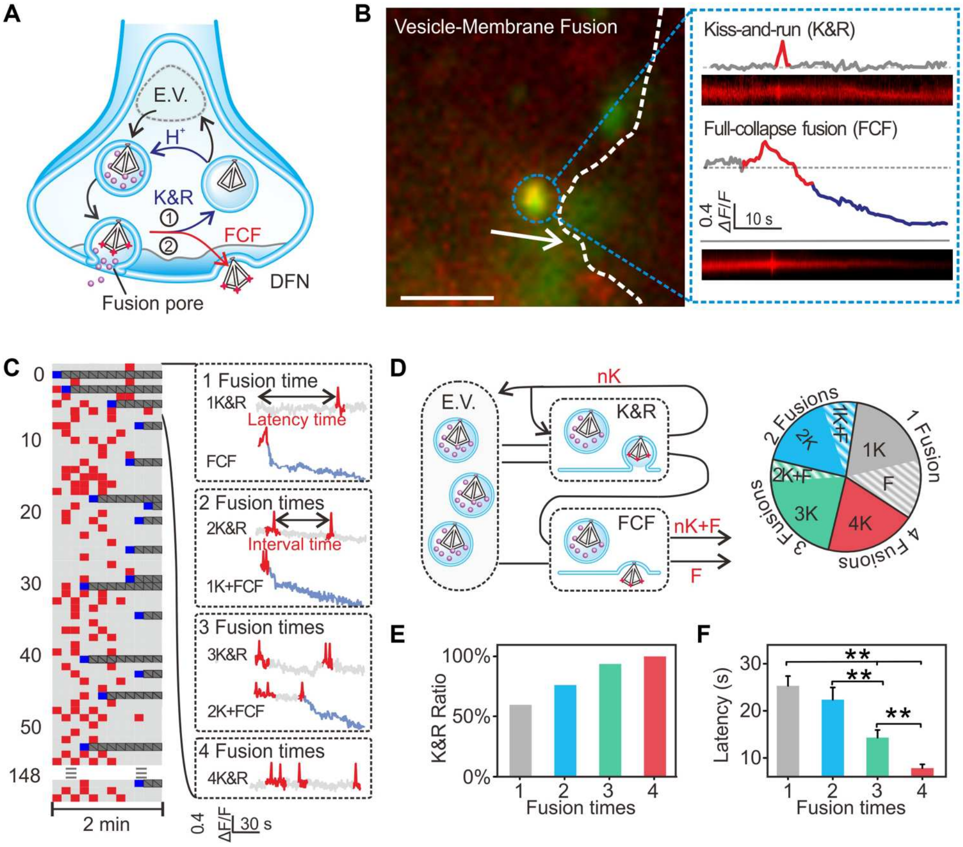

**Fig. 6. Vesicle fusion dynamics of DFNs.** (**A**) DFNs probe vesicle fusion dynamics. The DFN-loaded endocytic vesicle (E.V.) moved to the cell membrane under $K^+$ stimulation. (**B**) TIRFM imaging of vesicle fusion and representative kymograph and the corresponding time-lapse fluorescence-intensity curves of two modes: K&R and FCF. Scale bar, 4 μm. (**C**) Raster representation of traces ($n$ = 148) from DFN-loaded vesicles that responded to high $K^+$ stimulation for 2 min. DFN signals registered as no response (gray), K&R (red), FCF (blue), or no longer present in the region of interest (black). (**D**) Scheme of vesicle fusion pattern and classification of vesicles with all fusion behaviors. Of the 412 vesicles, 148 fused upon high $K^+$ stimulation. (**E**) K&R ratio of single fusion (gray), two fusions (blue), three fusions (green), and four fusions (red). (**F**) Average latency of the first fusion [25.32, 22.37, 14.33, and 7.83 s for single fusion (gray, $n$ = 47), two fusions (blue, $n$ = 35), three fusions (green, $n$ = 37), and four fusions (red, $n$ = 29), respectively]. The error bars represent mean + SEM. $^{**}P < 0.01$, unpaired two-sample $t$ test.

functions of a natural nanomachine to control and sense the dynamic behavior of nanosystems in an efficient and selective manner. It would be a substantial development if such DFNs were tailored to be more tissue- or cell-specific to expand their application range (*33*). The programmability and robustness of DFNs provide a promising approach for sensing, diagnostics, and therapies in living systems.

## MATERIALS AND METHODS

### Reagents

Fluorescently modified oligonucleotides were obtained from Invitrogen (Shanghai, China) and purified by high-performance liquid chromatography. Other oligonucleotides were purchased from Shanghai Sangong Biotech and purified by polyacrylamide gel electrophoresis (PAGE). The DNA sequences used are listed in tables S1 to S3. Single-stranded scaffold M13mp18 DNA was obtained from New England Biolabs. SEP was obtained from Shanghai Sangong Biotech. For more information, please see Supplementary Methods S1.

### Preparation of TDF-based DFNs

TDFs with length edges of 7, 20, and 26 bp were assembled by mixing equimolar strands in Tris–magnesium chloride (TM) buffer (20 mM Tris and 50 mM $MgCl_2$ at pH 8.0) in 1 μM. The mixtures were heated to 95°C for 5 min and then cooled to 4°C in 60 s using a Peltier Mode PTC-200 thermal cycler (MJ Research Inc., SA). The 8% PAGE in 0.5 × Tris-boric acid–EDTA buffer [45 mM Tris, 45 mM boric acid, and 1 mM EDTA (pH 8.0)] was run at a constant voltage of 80 V for 2 hours. The 120-bp TDF (DNA origami tetrahedron) was prepared according to published work (*53*). The staple DNA strands (50 nM) and M13mp18 scaffold DNA strands (10 nM) were mixed in a molar ratio of 5:1 in 1 × TAE buffer [40 mM Tris, 2 mM EDTA, 20 mM acetic acid, and 12.5 mM $MgAc_2$ (pH 8.0)], and the mixture was cooled from 95° to 20°C at a rate of 0.1°C/min. To remove excess staples of origami, we washed the prepared samples two times with the 1 × TAE buffer using Amicon Ultra 0.5-ml centrifugal filters (molecular weight cutoff, 100 kDa) at a speed of 3000$g$ for 10 min. The 1.5% agarose gel electrophoresis was run at 80 V in 1 × TAE buffer for 30 min.

### Preparation of DFN-AuNPs

For the distance change experiment, 5-nm AuNPs were used, whereas 10-nm AuNPs were used for the endocytosis experiment. AuNPs were first modified with Bis(*p*-sulfonatophenyl)phenylphosphine dihydrate dipotassium salt stabilizers according to published work (*54*). Next, thiol-link strand was added to the solution with a molar ratio of DNA/AuNPs = 200, and the mixture was slowly brought up (1-hour incubation, five times) by adding citrate-HCl buffer (100 mM, pH 3.0) to the solution to a final citrate concentration of 50 mM. The solution was recollected and then centrifuged (10,000*g*, 30 min) to acquire the DNA-AuNPs, which were subsequently resuspended in phosphate-buffered saline (PBS) buffer and quantified by ultraviolet-visible (UV-vis) absorption spectrophotometer at 520 nm. For the distance change experiment, the DFN was added to the DNA-AuNP solution with a molar ratio of DFN/DNA-AuNPs = 0.5, and for the endocytosis experiment, the DFN was added to the DNA-AuNP solution with a molar ratio of DFN/DNA-AuNPs = 20. Sample conjugates containing 50% sucrose (10 μl) were added to the lane, and the 1.5% agarose gel electrophoresis was run at 100 V in 1 × TAE buffer for 30 min.

### AFM imaging

3-Aminopropyltriethoxysilane (0.5%, 10 μl) was dropped and incubated on freshly cleaved mica for 2 min. Then, mica was washed three times with Milli-Q water and dried with $N_2$ air. TDF samples (10 μl) were incubated for 5 min on treated mica and washed with Milli-Q water, and TM buffer was added. The sample was scanned in Cypher VRS (Asylum Research) using AC10DS tips (Olympus). Typical scanning parameters were scan rate = 30 Hz, lines = 512, amplitude setpoint = 150 to 300 mV, and drive amplitude = 180 to 300 mV.

### Single-molecule imaging

TIRFM imaging was performed on a commercial superresolution microscope (N-STORM, Nikon) with a 100× objective lens [numerical aperture (NA), 1.49] and an electron multiplying charge-coupled device (EMCCD) camera (Andor, iXon 3). A clean glass coverslip was modified with the mixture of polyethylene glycol (PEG) and biotin-PEG for 2 hours. Streptavidin was then adsorbed on the coverslip for 30 min. Next, the biotinylated DFN-2 (10 pM) was immobilized on the coverslip for 30 min. For FRET, a 561-nm solid-state laser (Coherent) was used to excite Cy3 and FRET channel successively.

### Fluorescence characterization in vitro

All fluorescence spectra were collected with a Hitachi F-4500 spectrophotometer equipped with a xenon lamp excitation source at 25°C. DFNs were used in 50 nM. SEP was used in 20 nM, and Qdot was used in 10 nM. DFN (1 μM) fluorescence was observed under UV light and imaged by the camera.

### CD spectroscopy

All CD spectroscopy was performed on a CD spectrometer (Applied Photophysics, UK) equipped with a temperature controller at 25°C. DFN and i-motif were used in 5 μM. The CD spectra were obtained from 260 to 320 nm with a 1 cm–by–1 cm quartz cuvette: data interval, 1 nm; scan speed, 20 nm/min; response time, 1 s. The baseline was collected using a control sample without DNA and subtracted from each spectrum for the DNA samples.

### Cell culture

PC12, Neuro-2a, and SH-SY5Y cells were all purchased from Shanghai Institute of Biological Sciences. All cells were cultured in RPMI 1640 medium (Invitrogen) supplemented with penicillin (100 U/ml; Invitrogen), streptomycin (100 mg/ml; Invitrogen), 2 mM L-glutamine (Invitrogen), and 10% heat-inactivated fetal bovine serum (FBS; Gibco) at 37°C in humidified air containing 5% $CO_2$. All cells were tested for mycoplasma before use in experiments. Cells were incubated with cholesterol-modified DNA for 2 min at room temperature and washed three times with PBS [10 mM phosphate buffer, 0.14 M NaCl, and 2.7 mM KCl (pH 7.4)] buffer. Then, cells were hybridized with complementary sequence or DFNs at 4°C for 15 min and washed three times with PBS buffer for confocal microscopy and flow cytometry experiments. For cells at the pH 5.5 experiment, PBS pH was set at 5.5 with HCl and NaOH. For DFN endocytosis, Tyrode stimulation solution with 3 μM FM 1-43 was incubated with cells for 5 min, washed 10 times with Tyrode solution, and then cultured in medium without FBS for 2 hours (DFN-3 for 2 or 5 hours). All cells were randomized for selection, and all cell experiments were performed blindly and with a minimum of three biological replicates.

### Cell labeling

Cells were incubated with cholesterol-modified DNA for 2 min at room temperature and washed three times with PBS [10 mM phosphate buffer, 0.14 M NaCl, and 2.7 mM KCl (pH 7.4)] buffer. Then, cells were hybridized with complementary sequence or DFNs at 4°C for 15 min and washed three times with PBS buffer for confocal microscopy and flow cytometry experiments. For cells at the pH 5.5 experiment, PBS pH was set at 5.5 with HCl and NaOH. For DFN endocytosis, Tyrode stimulation solution with 3 μM FM 1-43 was incubated with cells for 5 min, washed 10 times with Tyrode solution, and then cultured in medium without FBS for 2 hours (DFN-3 for 2 or 5 hours).

### CLSM imaging

Images of fluorescently stained cells were obtained with a TCS SP8 confocal microscope. Complementary sequence and DFN were excited with a 633- or 561-nm laser; FM 1-43 was excited with a 488-nm laser. The image analysis was performed using ImageJ software.

### Flow cytometry

Cells were labeled with complementary sequence or DFN and then washed three times with PBS buffer. Next, 0.2 ml of trypsin (Invitrogen) was added. Then, 0.5 ml of RPMI 1640 was added, and the resulting cell suspensions were collected into tubes. At least 5000 cells were analyzed using a FACS Calibur flow cytometer (BD Biosciences).

### TEM imaging

For the distance change experiment, 20 nM DFN-AuNP (5 nm) solution (10 μl) was directly deposited on the grid for 10 min, and excess solution was wicked away with filter paper. The grid was washed two times by Milli-Q water and then submitted for TEM characterization. Imaging was performed using a TEM (Talos

L120C G2, Thermo Fisher Scientific, USA) operated at an acceleration voltage of 120 kV.

For the endocytosis experiment, PC12 cells were incubated with cholesterol-modified DNA for 2 min at room temperature, washed three times with 1 × PBS, and then treated with 5 nM DFN-AuNPs (10 nm) for 12 hours in FBS-free medium. At the end of incubation, excess solution was removed. Next, cells were collected into cell pellets, fixed with 2.5% glutaraldehyde in PBS at 4°C overnight, and further fixed with 1% $OsO_4$. After gradual dehydration was performed with ethanol and acetone, cell pellets were embedded in Epon 812 resins (Electron Microscopy Science), sliced to pieces with a thickness of 70 nm, and then stained with uranyl acetate. Images of cell slices were taken with Talos L120C G2 TEM using a beam voltage of 120 kV.

## Vesicle dynamics monitoring and image analysis

All TIRFM experiments were conducted on a commercial total internal reflection fluorescence microscope (N-STORM, Nikon) with a 100× objective lens (NA, 1.49) and an electron EMCCD camera (Andor, iXon 3). A 488-nm (100 mW) and a 647-nm (different energy for different experiments) solid-state laser (Coherent) were used for exciting FM 1-43 and Alexa 647, respectively.

For imaging DFNs in vesicles, we used a total internal reflection fluorescence mode. For probing vesicle fusion dynamics, we used wide-field mode to minimize any effects of possible variations in *z* distance, and the 640-nm laser is low energy to avoid photobleaching. For vesicle fusion, high $K^+$ stimulation was used. Dynamic experiments were generally carried out (exposure time = 30 ms per frame) for 2 min.

The image analysis procedures were carried out with ImageJ software, and the dates were analyzed with Origin. Fluorescence intensity should subtract blank to correct bleaching. For probing vesicle fusion dynamics, to avoid spurious events arising from background noise, positive deflections were only defined as more than 2.5 times the SD of baseline during no high $K^+$ stimulation, and negative deflections were analyzed only if they fell after a positive deflection (*44*, *55*).

## Statistical analysis

Two-tailed, Student's *t* test was used and performed in Origin (student version) for all experiments. The results were reported as means ± SD or mean ± SEM. Statistical significance was indicated as $^{**}P < 0.01$. No data were excluded from the analysis, and samples were randomly allocated to different groups. The smooth kernel distribution of data points was shown in violin plots.

## Supplementary Materials

**This PDF file includes:**
Tables S1 to S3
Supplementary Methods S1
Figs. S1 to S45

**Other Supplementary Material for this manuscript includes the following:**
MDAR Reproducibility Checklist

## REFERENCES AND NOTES

1. M. A. McEvoy, N. Correll, Materials that couple sensing, actuation, computation, and communication. *Science* **347**, 1261689 (2015).
2. E. M. Leung, M. Colorado Escobar, G. T. Stiubianu, S. R. Jim, A. L. Vyatskikh, Z. Feng, N. Garner, P. Patel, K. L. Naughton, M. Follador, E. Karshalev, M. D. Trexler, A. A. Gorodetsky, A dynamic thermoregulatory material inspired by squid skin. *Nat. Commun.* **10**, 1947 (2019).
3. D. Hwang, E. J. Barron, A. B. M. Tahidul Haque, M. D. Bartlett, Shape morphing mechanical metamaterials through reversible plasticity. *Sci. Robot.* **7**, eabg2171 (2022).
4. G. Picardi, M. Chellapurath, S. Iacoponi, S. Stefanni, C. Laschi, M. Calisti, Bioinspired underwater legged robot for seabed exploration with low environmental disturbance. *Sci. Robot.* **5**, eaaz1012 (2020).
5. C. Xu, G. T. Stiubianu, A. A. Gorodetsky, Adaptive infrared-reflecting systems inspired by cephalopods. *Science* **359**, 1495–1500 (2018).
6. Y. Jin, Y. Lin, A. Kiani, I. D. Joshipura, M. Ge, M. D. Dickey, Materials tactile logic via innervated soft thermochromic elastomers. *Nat. Commun.* **10**, 4187 (2019).
7. F. Alber, S. Dokudovskaya, L. M. Veenhoff, W. Zhang, J. Kipper, D. Devos, A. Suprapto, O. Karni-Schmidt, R. Williams, B. T. Chait, A. Sali, M. P. Rout, The molecular architecture of the nuclear pore complex. *Nature* **450**, 695–701 (2007).
8. C. Strambio-De-Castillia, M. Niepel, M. P. Rout, The nuclear pore complex: Bridging nuclear transport and gene regulation. *Nat. Rev. Mol. Cell Biol.* **11**, 490–501 (2010).
9. M. Beck, E. Hurt, The nuclear pore complex: Understanding its function through structural insight. *Nat. Rev. Mol. Cell Biol.* **18**, 73–89 (2017).
10. S. Takamori, M. Holt, K. Stenius, E. A. Lemke, M. Gronborg, D. Riedel, H. Urlaub, S. Schenck, B. Brugger, P. Ringler, S. A. Muller, B. Rammner, F. Grater, J. S. Hub, B. L. De Groot, G. Mieskes, Y. Moriyama, J. Klingauf, H. Grubmuller, J. Heuser, F. Wieland, R. Jahn, Molecular anatomy of a trafficking organelle. *Cell* **127**, 831–846 (2006).
11. G. W. Gould, J. L. Schwartz, New roles for endosomes: From vesicular carriers to multipurpose platforms. *Nat. Rev. Mol. Cell Biol.* **10**, 287–292 (2009).
12. B. G. Wilhelm, S. Mandad, S. Truckenbrodt, K. Kröhnert, C. Schäfer, B. Rammner, S. L. Koo, G. A. Claßen, M. Krauss, V. Haucke, H. Urlaub, S. O. Rizzoli, Composition of isolated synaptic boutons reveals the amounts of vesicle trafficking proteins. *Science* **344**, 1023–1028 (2014).
13. T. C. Sudhof, Neurotransmitter release: The last millisecond in the life of a synaptic vesicle. *Neuron* **80**, 675–690 (2013).
14. G. Raposo, W. Stoorvogel, Extracellular vesicles: Exosomes, microvesicles, and friends. *J. Cell Biol.* **200**, 373–383 (2013).
15. S. Modi, S. M G, D. Goswami, G. D. Gupta, S. Mayor, Y. Krishnan, A DNA nanomachine that maps spatial and temporal pH changes inside living cells. *Nat. Nanotechnol.* **4**, 325–330 (2009).
16. S. Modi, C. Nizak, S. Surana, S. Halder, Y. Krishnan, Two DNA nanomachines map pH changes along intersecting endocytic pathways inside the same cell. *Nat. Nanotechnol.* **8**, 459–467 (2013).
17. D. Bhatia, S. Arumugam, M. Nasilowski, H. Joshi, C. Wunder, V. Chambon, V. Prakash, C. Grazon, B. Nadal, P. K. Maiti, L. Johannes, B. Dubertret, Y. Krishnan, Quantum dot-loaded monofunctionalized DNA icosahedra for single-particle tracking of endocytic pathways. *Nat. Nanotechnol.* **11**, 1112–1119 (2016).
18. K. Leung, K. Chakraborty, A. Saminathan, Y. Krishnan, A DNA nanomachine chemically resolves lysosomes in live cells. *Nat. Nanotechnol.* **14**, 176–183 (2019).
19. L. Liang, J. Li, Q. Li, Q. Huang, J. Shi, H. Yan, C. Fan, Single-particle tracking and modulation of cell entry pathways of a tetrahedral DNA nanostructure in live cells. *Angew. Chem. Int. Ed.* **53**, 7745–7750 (2014).
20. S. Ohta, D. Glancy, W. C. W. Chan, DNA-controlled dynamic colloidal nanoparticle systems for mediating cellular interaction. *Science* **351**, 841–845 (2016).
21. C. Cui, K. Chakraborty, X. A. Tang, K. Q. Schoenfelt, A. Hoffman, A. Blank, B. McBeth, N. Pulliam, C. A. Reardon, S. A. Kulkarni, T. Vaisar, A. Ballabio, Y. Krishnan, L. Becker, A lysosome-targeted DNA nanodevice selectively targets macrophages to attenuate tumours. *Nat. Nanotechnol.* **16**, 1394–1402 (2021).
22. J. Bongard, Morphological change in machines accelerates the evolution of robust behavior. *Proc. Natl. Acad. Sci. U.S.A.* **108**, 1234–1239 (2011).
23. S. A. Morin, R. F. Shepherd, S. W. Kwok, A. A. Stokes, A. Nemiroski, G. M. Whitesides, Camouflage and display for soft machines. *Science* **337**, 828–832 (2012).
24. Y. Zhao, C. Lo, L. Ruan, C. Pi, C. Kim, Y. Alsaid, I. Frenkel, R. Rico, T. Tsao, X. He, Somatosensory actuator based on stretchable conductive photothermally responsive hydrogel. *Sci. Robot.* **6**, eabd5483 (2021).
25. C. Larson, B. Peele, S. Li, S. Robinson, M. Totaro, L. Beccai, B. Mazzolai, B. Shepherd, Highly stretchable electroluminescent skin for optical signaling and tactile sensing. *Science* **351**, 1071–1074 (2016).

26. M. Wehner, R. L. Truby, D. J. Fitzgerald, B. Mosadegh, G. M. Whitesides, J. A. Lewis, R. J. Wood, An integrated design and fabrication strategy for entirely soft, autonomous robots. *Nature* **536**, 451–455 (2016).
27. S. Krause, B. L. Feringa, Towards artificial molecular factories from framework-embedded molecular machines. *Nat. Rev. Chem.* **4**, 550–562 (2020).
28. T. Nitta, Y. Wang, Z. Du, K. Morishima, Y. Hiratsuka, A printable active network actuator built from an engineered biomolecular motor. *Nat. Mater.* **20**, 1149–1155 (2021).
29. E. Kopperger, J. List, S. Madhira, F. Rothfischer, D. C. Lamb, F. C. Simmel, A self-assembled nanoscale robotic arm controlled by electric fields. *Science* **359**, 296–301 (2018).
30. A. Cangialosi, C. Yoon, J. Liu, Q. Huang, J. Guo, T. D. Nguyen, D. H. Gracias, R. Schulman, DNA sequence–directed shape change of photopatterned hydrogels via high-degree swelling. *Science* **357**, 1126–1130 (2017).
31. T. Gerling, K. F. Wagenbauer, A. M. Neuner, H. Dietz, Dynamic DNA devices and assemblies formed by shape-complementary, non–base pairing 3D components. *Science* **347**, 1446–1452 (2015).
32. D. Zhu, H. Pei, G. Yao, L. Wang, S. Su, J. Chao, L. Wang, A. Aldalbahi, S. Song, J. Shi, J. Hu, C. Fan, X. Zuo, A surface-confined proton-driven DNA pump using a dynamic 3D DNA scaffold. *Adv. Mater.* **28**, 6860–6865 (2016).
33. S. Dey, C. Fan, K. V. Gothelf, J. Li, C. Lin, L. Liu, N. Liu, M. A. D. Nijenhuis, B. Saccà, F. C. Simmel, H. Yan, P. Zhan, DNA origami. *Nat. Rev. Methods Primers* **1**, 13 (2021).
34. S. Hamada, K. G. Yancey, Y. Pardo, M. Gan, M. Vanatta, D. An, Y. Hu, T. L. Derrien, R. Ruiz, P. Liu, J. Sabin, D. Luo, Dynamic DNA material with emergent locomotion behavior powered by artificial metabolism. *Sci. Robot.* **4**, eaaw3512 (2019).
35. J. Wang, Y. Li, G. Nie, Multifunctional biomolecule nanostructures for cancer therapy. *Nat. Rev. Mater.* **6**, 766–783 (2021).
36. Q. Chen, F. Ding, S. Zhang, Q. Li, X. Liu, H. Song, X. Zuo, C. Fan, S. Mou, Z. Ge, Sequential therapy of acute kidney injury with a DNA nanodevice. *Nano Lett.* **21**, 4394–4402 (2021).
37. C. Wiraja, Y. Zhu, D. C. S. Lio, D. C. Yeo, M. Xie, W. Fang, Q. Li, M. Zheng, M. Van Steensel, L. Wang, C. Fan, C. Xu, Framework nucleic acids as programmable carrier for transdermal drug delivery. *Nat. Commun.* **10**, 1147 (2019).
38. D. Jiang, Z. Ge, H. J. Im, C. G. England, D. Ni, J. Hou, L. Zhang, C. J. Kutyreff, Y. Yan, Y. Liu, S. Y. Cho, J. W. Engle, J. Shi, P. Huang, C. Fan, H. Yan, W. Cai, DNA origami nanostructures can exhibit preferential renal uptake and alleviate acute kidney injury. *Nat. Biomed. Eng.* **2**, 865–877 (2018).
39. D. Bhatia, S. Surana, S. Chakraborty, S. P. Koushika, Y. Krishnan, A synthetic icosahedral DNA-based host-cargo complex for functional *in vivo* imaging. *Nat. Commun.* **2**, 339 (2011).
40. K. Gehring, J. L. Leroy, M. Guéron, A tetrameric DNA structure with protonated cytosine-cytosine base pairs. *Nature* **363**, 561–565 (1993).
41. D. Liu, S. Balasubramanian, A proton-fuelled DNA nanomachine. *Angew. Chem. Int. Ed.* **42**, 5734–5736 (2003).
42. S. He, M. Liu, F. Yin, J. Liu, Z. Ge, F. Li, M. Li, J. Shi, L. Wang, X. Mao, X. Zuo, Q. Li, Programming folding cooperativity of the dimeric i-motif with DNA frameworks for sensing small pH variations. *Chem. Commun.* **57**, 3247–3250 (2021).
43. M. A. Gaffield, W. J. Betz, Imaging synaptic vesicle exocytosis and endocytosis with FM dyes. *Nat. Protoc.* **1**, 2916–2921 (2006).
44. Q. Zhang, Y. Li, R. W. Tsien, The dynamic control of kiss-and-run and vesicular reuse probed with single nanoparticles. *Science* **323**, 1448–1453 (2009).
45. M. Lindau, W. Almers, Structure and function of fusion pores in exocytosis and ectoplasmic membrane fusion. *Curr. Opin. Cell Biol.* **7**, 509–517 (1995).
46. B. P. Jena, Fusion pore in live cells. *News Physiol. Sci.* **17**, 219–222 (2002).
47. R. Jahn, D. Fasshauer, Molecular machines governing exocytosis of synaptic vesicles. *Nature* **490**, 201–207 (2012).
48. L. He, X. S. Wu, R. Mohan, L. G. Wu, Two modes of fusion pore opening revealed by cell-attached recordings at a synapse. *Nature* **444**, 102–105 (2006).
49. A. Liu, X. Huang, W. He, F. Xue, Y. Yang, J. Liu, L. Chen, L. Yuan, P. Xu, pHmScarlet is a pH-sensitive red fluorescent protein to monitor exocytosis docking and fusion steps. *Nat. Commun.* **12**, 1413 (2021).
50. X. Gao, W. C. Chan, S. Nie, Quantum-dot nanocrystals for ultrasensitive biological labeling and multicolor optical encoding. *J. Biomed. Opt.* **7**, 532–537 (2002).
51. Q. Zhang, Y. Q. Cao, R. W. Tsien, Quantum dots provide an optical signal specific to full collapse fusion of synaptic vesicles. *Proc. Natl. Acad. Sci. U.S.A.* **104**, 17843–17848 (2007).
52. H. Park, Y. Li, R. W. Tsien, Influence of synaptic vesicle position on release probability and exocytotic fusion mode. *Science* **335**, 1362–1366 (2012).
53. W. Liu, M. Tagawa, H. L. Xin, T. Wang, H. Emamy, H. Li, K. G. Yager, F. W. Starr, A. V. Tkachenko, O. Gang, Diamond family of nanoparticle superlattices. *Science* **351**, 582–586 (2016).
54. R. J. Macfarlane, B. Lee, M. R. Jones, N. Harris, G. C. Schatz, C. A. Mirkin, Nanoparticle superlattice engineering with DNA. *Science* **334**, 204–208 (2011).
55. C. Cali, J. Marchaland, R. Regazzi, P. Bezzi, SDF 1-alpha (CXCL12) triggers glutamate exocytosis from astrocytes on a millisecond time scale: Imaging analysis at the single-vesicle level with TIRF microscopy. *J. Neuroimmunol.* **198**, 82–91 (2008).
56. A. Phan, M. Gueron, J. L. Leroy, The solution structure and internal motions of a fragment of the cytidine-rich strand of the human telomere. *J. Mol. Biol.* **299**, 123–144 (2000).

**Acknowledgments**

**Funding:** This work was financially supported by the NSFC (T2188102, 22025404, 22174092, and 21991134), National Key R&D Program of China (2021YFF1200300), the Natural Science Foundation of Shanghai (19JC1410300 and 21ZR1439600), the Innovative Research Team of High-Level Local Universities in Shanghai (SHSMU-ZLCX20212602), and the K. C. Wong Foundation at Shanghai Jiao Tong University. **Author contributions:** C.F. and X.Z. directed the research. C.F., X.Z., and X.M. conceived the project. J. Liu performed the research. X.J. assisted with the AFM imaging. J. Liu, M. Liu, F.L., M. Li, Q.L., J.S., J. Li, and L.W. analyzed the data. All authors discussed the results and commented on the manuscript. C.F., X.Z., X.M., and J. Liu cowrote the paper. **Competing interests:** The authors declare that they have no competing interests. **Data and materials availability:** All data needed to evaluate the conclusions in the paper are included in the main text or Supplementary Materials. The data for this study have been deposited in the Dataverse database (https://doi.org/10.7910/DVN/4S5Q2O).

Submitted 15 April 2022
Resubmitted 01 September 2022
Accepted 22 November 2022
Published 21 December 2022
10.1126/scirobotics.abq5151

Science Robotics

# Mechano-fluorescence actuation in single synaptic vesicles with a DNA framework nanomachine

Jiangbo Liu, Xinxin Jing, Mengmeng Liu, Fan Li, Min Li, Qian Li, Jiye Shi, Jiang Li, Lihua Wang, Xiuhai Mao, Xiaolei Zuo, and Chunhai Fan

*Sci. Robot.* **7** (73), eabq5151. DOI: 10.1126/scirobotics.abq5151

---

*Science Robotics* (ISSN 2470-9476) is published by the American Association for the Advancement of Science. 1200 New York Avenue NW, Washington, DC 20005. The title *Science Robotics* is a registered trademark of AAAS.